Provided for non-commercial research and education use.
Not for reproduction, distribution or commercial use.

This article appeared in a journal published by Elsevier. The attached copy is furnished to the author for internal non-commercial research and education use, including for instruction at the authors institution and sharing with colleagues.

Other uses, including reproduction and distribution, or selling or licensing copies, or posting to personal, institutional or third party websites are prohibited.

In most cases authors are permitted to post their version of the article (e.g. in Word or Tex form) to their personal website or institutional repository. Authors requiring further information regarding Elsevier's archiving and manuscript policies are encouraged to visit:

http://www.elsevier.com/authorsrights

Author's personal copy

Journal of Sound and Vibration 332 (2013) 5566–5583

Contents lists available at SciVerse ScienceDirect

Journal of Sound and Vibration

journal homepage: www.elsevier.com/locate/jsvi

A multi-scale pseudo-force model for characterization of damage in beam components with unknown material and structural parameters

Maosen Cao [a,b], Zhongqing Su [c], Li Cheng [a,c,*], Hao Xu [a,c]

[a] The Hong Kong Polytechnic University, Shenzhen Research Institute, Shenzhen 518057, PR China
[b] Department of Engineering Mechanics, College of Mechanics & Materials, The Hohai University, Nanjing, 210098, People's Republic of China
[c] Department of Mechanical Engineering, The Hong Kong Polytechnic University, Hung Hom, Kowloon, Hong Kong Special Administrative Region

ARTICLE INFO

Article history:
Accepted 3 May 2013
Handling Editor: I. Trendafilova
Available online 10 June 2013

ABSTRACT

Most existing damage characterization exercises require explicitly defined material properties, geometric parameters and boundary conditions of the object to be evaluated. However, satisfying such a rudimental prerequisite can be a challenging task in reality. It may be somewhat difficult or even impossible to exactly acquire these parameters beforehand in some occasions, especially when the object comprises various structural components of distinct material/geometric properties and different boundary conditions. A damage characterization strategy, residing on a multi-scale pseudo-force damage model, was developed with an aim of achieving robust damage evaluation by tolerating ignorance of the knowledge on partial material/structural properties and boundary conditions of the object *a priori*. Proof-of-concept validation was carried out numerically and experimentally by characterizing a fine crack in an Euler–Bernoulli beam, a structural component included in a system with irregular boundaries, without knowing its material and structural parameters beforehand. Exact characterization results demonstrated the effectiveness and accuracy of the proposed approach.

© 2013 Elsevier Ltd. All rights reserved.

1. Introduction

Damage characterization has been practiced over the years, leading to a large variety of well-defined nondestructive evaluation (NDE) techniques, as typified by radioscopy, ultrasonic inspection, shearography, magnetic resonance imagery, laser interferometry, acoustic emission, thermography, eddy-current, *etc.* [1–3]. These mature techniques can be very effective in locally evaluating damage of a small structural fragment in an offline manner. Targeted at a continuous and automated evaluation, at an overall system level, so as to be conducive to online damage characterization, structural health monitoring (SHM) technique has been entailed, enjoying burgeoning development in the past two decades. Intensive efforts in this field have put such a technique on the verge of practical engineering applications [4–10].

Most SHM techniques were developed based on quantifying the singularities in either global vibration responses [9,11–14] or local elastic waves [1,15–27], when compared with benchmark signals. The former holds the premise that the occurrence of

* Corresponding author at: Department of Mechanical Engineering, Hong Kong Polytechnic University, Hung Hom, Kowloon, Hong Kong Special Administrative Region. Tel.: +85 227 666 769; fax: +85 223 654 703.
E-mail address: li.cheng@polyu.edu.hk (L. Cheng).

0022-460X/$ - see front matter © 2013 Elsevier Ltd. All rights reserved.
http://dx.doi.org/10.1016/j.jsv.2013.05.002

Author's personal copy

damage induces changes in physical properties of the structure under inspection (*e.g.*, local stiffness, density, mass, thermal properties, and electromechanical impedance), and these changes are in turn manifested in global dynamic responses captured from the structure; while the latter explores differences in acquired wave scattering phenomena (*e.g.*, wave reflection, transmission, refraction and diffraction), mode conversion and energy absorption, upon interaction of the incident waves with damage. Both detection philosophies require benchmark counterparts or pre-developed global models, from which baseline signals can be obtained for comparison. They rely on well-controlled excitation sources for generating structural vibration or activating elastic waves. Most rudimentarily, the majority of the approaches in the above two categories require prior knowledge on the basic material properties (*e.g.*, elastic modulus, density and Poisson's ratio), geometric features (*e.g.*, dimension of cross-section) and deterministic boundary conditions of the object under inspection, so as to accurately calibrate some prerequisite parameters for implementation (*e.g.*, wave propagation velocity, and damping ratio).

However it is envisaged that acquiring all these prerequisites beforehand can be a highly tanglesome or even impossible task in engineering practice. For instance, it is somewhat difficult to obtain the accurate modulus of elasticity for an in-service metallic structure in a harsh working environment when it bears corrosion. On the other hand, this can also be a ubiquitous concern in applications where the object to be inspected comprises structural components of different types, distinct material properties, various geometric parameters and diverse boundary conditions. Such a constraint hampers the real-world applications of many NDE and SHM techniques. To overcome such a problem, efforts have been made, resulting in two major groups of approaches: the one using the curvature shape [28–31] and that capitalizing on continuous wavelet transform (CWT)-based signal processing [32–37]. The former correlates damage-induced changes in the stiffness of the structure with the singularity detected in experimentally captured structural deflection. Quantifying such a singularity can lead to the detection of the damage in a spatial domain. Approaches in the latter group calculate CWT coefficients of experimentally captured transverse deflection, which can become abnormal in the space-scale domain if damage occurs. For both groups, information on the material properties or geometric parameters is not required *a priori*. However, most of these methods rely substantially on signal processing techniques (whereby to detect the singularity in a signal), without a solid cornerstone of mechanics to link the essential features of damage to the changes in signals, therefore defining damage without explicit physical implications.

In the present work, a damage characterization approach was developed, able to tolerate the absence of knowledge on partial connatural properties of the object to be inspected, so as to enhance the robustness and practicability of damage characterization in engineering practice. The approach was formulated based on a multi-scale pseudo-force damage model developed by the authors in their previous work [38]. This damage model, canvassing damage-caused local perturbation to higher-order dynamic equilibrium characteristics, is able to depict fine damage in a structural component, while tactically avoiding the reliance on benchmark structures, baseline signals, global model, modal information, boundary conditions and rigorous excitation sources. However, material and geometric parameters of the component under inspection are of necessity for developing the model. Residing on such a damage model, this paper proposed a new approach to further eliminate the requirement of prior knowledge on material and geometric parameters.

Without loss of generality, an Euler–Bernoulli beam component (EBC) was selected for illustration purpose. The outline of the paper is as follows. Section 2 briefs the essence of the multi-scale pseudo-force damage model, based on which the proposed methodology was developed. Principle of the approach is elaborated in Section 3. As proof-of-concept validation, the approach was verified by characterizing a fine crack in an EBC numerically and experimentally, reported in Sections 4 and 5, respectively.

2. Multi-scale pseudo-force damage model

In authors' previous work [38], a *Multi-scale Pseudo-force Damage Model* (MPDM) in the wavelet domain was developed. By analytically calibrating the damage-caused local perturbation to dynamic equilibrium characteristics of a structural component, the model claims explicit physical and mechanics foundations. Different from a signal processing technique, it renders a practical solution to multi-scale modeling and identification of damage.

2.1. Model development

To illustrate the approach, consider an irregular structure with complex boundaries as shown in Fig. 1(a), which contains multiple cracks scattered in a multitude of EBCs. Let us focus on a typical EBC of l in its length, bearing a fine double-edged crack located at ξ, as shown in Fig. 1(b). Here, '*fine*' means the width of the crack is ignorable along the beam span. In the coordinate system shown in Fig. 1(b), this cracked EBC can be defined as [38]

$$E_0 I_0 \frac{\mathrm{d}^4 W(x)}{\mathrm{d}x^4} - \rho_0 A_0 \omega^2 W(x) = \left[r_1 E_0 I_0 \frac{\mathrm{d}^4 W(x)}{\mathrm{d}x^4} - r_2 \rho_0 A_0 \omega^2 W(x) \right] \delta(x-\xi), \tag{1}$$

where $W(x)$ denotes the transverse displacement of the EBC vibrating at a frequency of ω; E_0, I_0, A_0 and ρ_0 are the modulus of elasticity, cross-sectional moment of inertia with regard to y-axis, area of the cross-section and material density (subscript '0' standing for a pristine status of the EBC without any damage). $r_1 = 1-(1-2e/h)^3$ and $r_2 = 2e/h$, which define the crack-caused

Author's personal copy

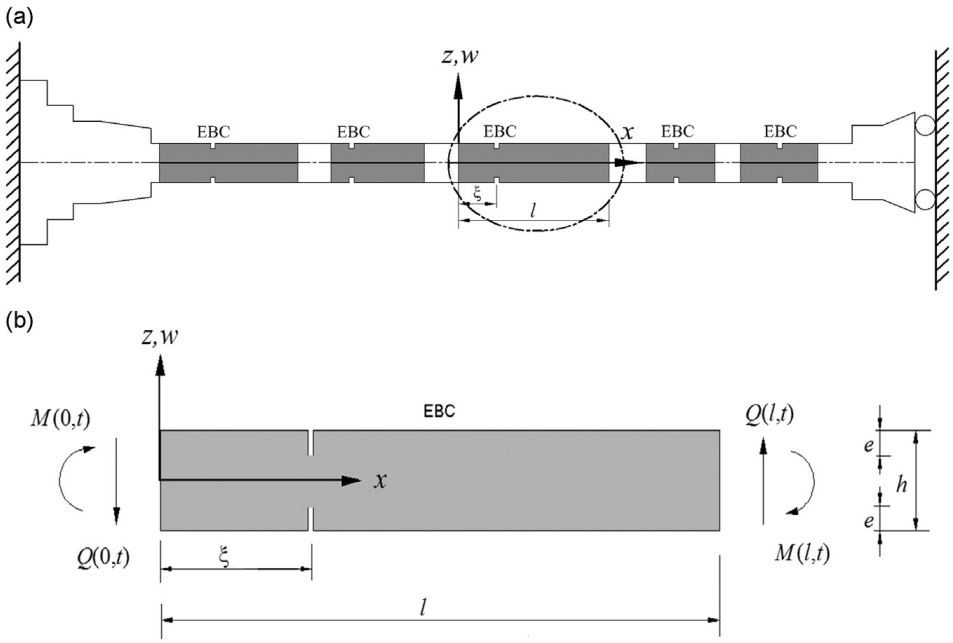

Fig. 1. (a) An irregular structure with complex boundaries containing multiple cracks scattered in a multitude of EBCs; (b) zoomed-in view of an EBC in the structure bearing a crack ($M(0,t)$ and $M(l,t)$: bending moments at $x=0$ and $x=l$ at moment t, respectively; $Q(0,t)$ and (l,t): shear forces at $x=0$ and $x=l$ at moment t, respectively).

reductions in the flexural stiffness and mass of the EBC, respectively (h is the height of the intact EBC and e is the depth of the crack at each side, see Fig. 1(b)). Note that r_1 and r_2 are not necessarily to be the same, and this allows certain flexibility in describing different damage scenarios (symmetrically double-edged, non-symmetrically double-edged or single-edged cracks). In particular, when either of r_1 or r_2 reduces to zero, the double-edged crack retreats to a single-edged crack. $\delta(x)$ is the Dirac function satisfying $f(x)\delta(x-\xi)=f(\xi)\delta(x-\xi)$ with $f(x)$ being an arbitrary function. With this property, Eq. (1) becomes

$$E_0I_0\frac{\mathrm{d}^4W(x)}{\mathrm{d}x^4}-\rho_0A_0\omega^2W(x)=\left[r_1E_0I_0\frac{\mathrm{d}^4W(x)}{\mathrm{d}x^4}\Big|_{x=\xi}-r_2\rho_0A_0\omega^2W(\xi)\right]\delta(x-\xi). \tag{2}$$

For convenience of discussion, let

$$\pi_{\mathrm{crack}}=r_1E_0I_0\frac{\mathrm{d}^4W(x)}{\mathrm{d}x^4}\Big|_{x=\xi}\delta(x-\xi) \text{ and } \Gamma_{\mathrm{crack}}=r_2\rho_0A_0\omega^2W(\xi)\delta(x-\xi). \tag{3}$$

Eq. (2) can then be re-written as

$$E_0I_0\frac{\mathrm{d}^4W(x)}{\mathrm{d}x^4}-\rho_0A_0\omega^2W(x)=\pi_{\mathrm{crack}}(x)-\Gamma_{\mathrm{crack}}(x)=\mathfrak{R}_{\mathrm{crack}}(x) \tag{4}$$

The right-hand-side term of Eq. (4) alludes to that the transverse vibration of an EBC containing a crack is equivalent to that of its intact counterpart subjected to a virtual force at the damage location ξ. This virtual force, denoted by $\mathfrak{R}_{\mathrm{crack}}(x)$, is called *pseudo-force* (*PF*) hereinafter, which comprises two crack-induced components: a *pseudo elastic force* (*PEF*) (*viz.*, $\pi_{\mathrm{crack}}(x)$ in Eq. (4)) and a *pseudo inertia force* (*PIF*) ($\Gamma_{\mathrm{crack}}(x)$ in Eq. (4)). Further letting $K=r_1E_0I_0(\mathrm{d}^4W(x)/\mathrm{d}x^4)|_{x=\xi}-r_2\rho_0A_0\omega^2W(\xi)$ yields a compact form of Eq. (2)

$$E_0I_0\frac{\mathrm{d}^4W(x)}{\mathrm{d}x^4}-\rho_0A_0\omega^2W(x)=\mathfrak{R}_{\mathrm{crack}}(x)=K\delta(x-\xi), \tag{5}$$

where K is associated with the severity of the crack. It is the concept of '*pseudo-force*' that names the model '*Pseudo-force Damage Model*'.

Based on Eq. (5), a damage characterization strategy was proposed: once $W(x)$ and the associated ω are obtained experimentally, and substituted to the left-hand side of Eq. (5), a residual (*i.e.*, the pseudo-force $\mathfrak{R}_{\mathrm{crack}}(x)$) emerges, which is expected to be prominent at the location of the crack (ξ). That is equivalent to a local perturbation (a pseudo-force exerted by the damage) to the dynamic equilibrium of the intact EBC. Such a residual manifests itself as a drastic change in the pattern of $\delta(x)$.

This model has been experimentally demonstrated [38] to outperform traditional vibration-based damage detection methods in several aspects including

Author's personal copy

(1) higher sensitivity to damage of tiny dimension, owing to the involvement of the fourth-order derivatives of equation of motion ($d^4W(x)/dx^4$);
(2) a point-by-point inspection manner at a local level, thus independent of any global model for the whole system;
(3) by the same token, no need for pre-knowledge on boundary conditions and modal information (complexity of the system would not limit the applicability of the approach);
(4) benefiting from its nature of local canvass and thus the independence of the rest of the inspection region, a capacity of characterizing multiple cracks (as illustrated in Fig. 1(a) where multiple EBCs are existent);
(5) no need for baseline signals, therefore immune from interference of fluctuating environmental factors such as temperature variation; and
(6) no specific requirement on excitation sources, as long as the component undergoes steady vibration (*e.g.*, under the normal operation of the system).

2.2. Model enhancement

However, the above model may not be sufficiently robust under noisy measurement conditions as a consequence of the high-order derivatives (mathematic processing of the differentiation ($d^4W(x)/dx^4$) may amplify noise components involved in $W(x)$ to a considerable level [31]). To enhance the robustness of the model towards practical implementation, the model defined by Eq. (5) was re-defined by converting it from a one-dimensional spatial space to a two-dimensional wavelet domain (s–u domain, where s and u are the *scale* (or *dilation*) and *space* (or *translation*) parameters, respectively) using a Gaussian wavelet transform [31,33,39,40]. This conversion is warranted by the properties of Gaussian wavelet transform, and the attribute of differentiation of convolution [41] described as

$$\frac{d}{du}(W*\overline{g}^p)(u)=\frac{dW}{dx}*\overline{g}^p(u)=W*\frac{d\overline{g}^p}{dx}(u) \tag{6}$$

where the asterisk denotes *convolution*; W is the abbreviated form for $W(x)$; and $\overline{g}^p$ for $\overline{g}^p(x)$, which is the conjugate of the pth-order Gaussian wavelet $g^p(x)$ (g^p for abbreviation); u is a variable generated upon convolution between W and $\overline{g}^p$, allowing $\int W(x)\overline{g}^p(u-x)dx=W*\overline{g}^p(u)$. With Eq. (6), the qth-order derivative of W can be obtained in terms of $\overline{g}^p$, as

$$\frac{d^qW}{dx^q}*\overline{g}_s^p(u)=W*\frac{d^q\overline{g}_s^p}{dx^q}(u)=\frac{C_p(-1)^ps^p}{C_{p+q}(-1)^{p+q}s^{p+q}}\,W*\overline{g}_s^{p+q}(u), \tag{7a}$$

where $\overline{g}_s^p(x)$ is the conjugate of $g_s^p(x)$ (the sub-wavelet of g^p at scale s), with the following property:

$$\overline{g}_s^p(x)=g_s^p(-x)=C_p(-1)^ps^p\frac{dg_s^0(-x)}{dx^p}, \tag{7b}$$

where $g^0(x)$ is the classical Gaussian function (g^0 for abbreviation), $g_s^0(x)$ is its sub-wavelet at scale s (g_s^0 for abbreviation), and C_p is a constant such that g^p satisfies the condition $\int_{-\infty}^{+\infty}(g^p)^2dx=1$. Eq. (7a) provides a Gaussian wavelet-based differential transform towards higher-order derivatives of W (*i.e.*, $d^4W(x)/dx^4$) in the model, by tactically differentiating g^p instead of W itself. Therefore, the amplification of measurement noise contained in W during differentiation can be circumvented. With the first-order Gaussian wavelet (g^1), the model in Eq. (5) can now be re-defined as

$$E_0I_0\frac{d^4W}{dx^4}*\overline{g}_s^1(u)-\rho_0A_0\omega^2W*\overline{g}_s^1(u)=K\overline{g}_s^1*\delta_\xi(u) \tag{8}$$

in which $\overline{g}_s^1*\delta_\xi(u)$ is the convolution between $\overline{g}_s^1(x)$ and $\delta(x-\xi)$, because $\delta(x-\xi)=\delta_\xi(x)$, a property of the Dirac function.

Further, noticing that

$$\overline{g}_s^1*\delta_\xi(u)=-g_s^1*\delta_\xi(u)\quad(\textit{from the property of Gaussian wavelet }\overline{g}_s^1(x)=g_s^1(-x)=-g_s^1(x)) \tag{9a}$$

and

$$f*\delta_\xi(u)=f(u-\xi)\quad(\textit{from the property of Dirac convolution between }\delta_\xi(x)\textit{ and any function }f(x)) \tag{9b}$$

one can obtain (for the right-hand term of Eq. (8))

$$\overline{g}_s^1*\delta_\xi(u)=-g_s^1*\delta_\xi(u)=-g_s^1(u-\xi). \tag{9c}$$

In addition, applying the operation defined by Eq. (7a) to $(d^4W/dx^4)*\overline{g}_s^1(u)$ in Eq. (8) yields

$$\frac{d^4W}{dx^4}*\overline{g}_s^1(u)=W*\frac{d^4\overline{g}_s^1}{dx^4}(u)=\frac{C_1(-1)^1s^1}{C_5(-1)^5s^5}W*\overline{g}_s^5(u)=\frac{1}{C_5s^4}W*\overline{g}_s^5(u) \tag{9d}$$

where C_1 and C_5 are two constants such that g^1 and g^5 satisfy conditions $\int_{-\infty}^{+\infty}(g^1)^2dx=1$ and $\int_{-\infty}^{+\infty}(g^5)^2dx=1$, respectively, leading to $C_1=1$ and $C_5=1/(3\sqrt{105})$.

Author's personal copy

Substituting Eqs. (9c) and (9d) into Eq. (8) gives rise to

$$\frac{1}{C_5 s^4} E_0 I_0 W * \bar{g}_s^5(u) - \rho_0 A_0 \omega^2 W * \bar{g}_s^1(u) = -K g_s^1(u-\xi), \tag{10a}$$

which can be re-arranged as

$$E_0 I_0 W * \bar{g}_s^5(u) - C_5 s^4 \rho_0 A_0 \omega^2 W * \bar{g}_s^1(u) = -C_5 s^4 K g_s^1(u-\xi). \tag{10b}$$

Letting $\tilde{K} = C_5 K$, Eq. (10b) becomes

$$E_0 I_0 W * \bar{g}_s^5(u) - C_5 s^4 \rho_0 A_0 \omega^2 W * \bar{g}_s^1(u) = -\tilde{K} s^4 g_s^1(u-\xi). \tag{11}$$

Eq. (11) is the transformed form of the pseudo-force damage model over a wavelet domain. Comparing Eq. (11) with Eq. (5), it can be seen that the *PEF*, *PIF* and *PF* terms in the model (described by Eq. (5)) are now deployed in a multi-scale form (associated with scale '*s*'). It can also be noticed that the *PF* term in the model is modulated by $-s^4$, presenting multi-scale features. Addressing such a multi-scale trait, Eq. (11) is further re-written in a compact form as

$$(M\_\mathrm{PEF}) - (M\_\mathrm{PIF}) = (M\_\mathrm{PF}), \tag{12a}$$

where

$$\begin{cases} M\_\mathrm{PEF} = E_0 I_0 W * \bar{g}_s^5(u) \\ M\_\mathrm{PIF} = C_5 s^4 \rho_0 A_0 \omega^2 W * \bar{g}_s^1(u) \\ M\_\mathrm{PF} = -\tilde{K} s^4 g_s^1(u-\xi). \end{cases} \tag{12b}$$

Eq. (12) is the enhanced version of the model. It explicitly reveals that damage in an EBC induces, virtually, a multi-scale pseudo-force (M_PF) that comprises two components: a multi-scale pseudo elastic force (M_PEF) and a multi-scale pseudo inertia force (M_PIF), where prefix '*M*' emphasizes the multi-scale attribute. Once a crack exists in the EBC, M_PF exhibits prominent changes at the crack location (ξ), and such changes take the pattern of $-s^4$-modulated $g_s^1(u-\xi)$ centered at $u=\xi$ [38]. The multi-scale nature of the MPDM empowers the damage identification with improved robustness under noisy measurement conditions.

By way of illustration, the MPDM constructed using Eq. (11) for an EBC containing a crack (crack parameters to be detailed in Section 4) is illustrated in Fig. 2(a–c) for the terms M_PEF, M_PIF and M_PF, respectively. Spanning a wide range of scales, the model is a multi-scale representation of the entire EBC over a space-scale domain. Furthermore, to facilitate exact ascertainment of the damage location, a spatial energy spectrum (SES)-based analysis was introduced, which is defined, at a given u (*i.e.*, at a given spatial location of the EBC of l in its length), as

$$\mathrm{SES}(u) = \frac{\int_\Theta [M\_\mathrm{PF}]^2 \mathrm{d}s}{\int_\Theta \int_0^l [M\_\mathrm{PF}]^2 \mathrm{d}u\, \mathrm{d}s} \tag{13}$$

where Θ is the scale range of interest. SES, varying with u, reflects a discrete distribution of the normalized signal energy over the wavelet domain along the EBC span. Benefiting from the mathematical operation of integral and squaring, changes in M_PF are strengthened exponentially in SES, contributing to the visualization of damage location in an enhanced representation. For illustration, the calculated SES for the above EBC is shown in Fig. 2(d), in which the location of the trough at $u=\xi$ between two adjacent peaks clearly points out the damage location. Nevertheless, it is noteworthy that explicitly defined material properties and geometric parameters of the EBC are prerequisites for establishing the above MPDM.

3. Damage characterization with unknown material and structural parameters

Residing on the MPDM, a damage characterization strategy was developed, able to tolerate the absence of prior knowledge on basic material properties, geometric features and boundary conditions of the object to be evaluated.

3.1. Principle

For illustration purpose and without loss of generality, let us use the same EBC and assume its basic material properties (E_0 and ρ_0), geometric parameters (I_0 and A_0) in the model (Eqs. (5) or (11)) and boundary conditions are unknown *a priori*. According to Eq. (11), the MPDM for the EBC is

$$E^* I^* W * \bar{g}_s^5(u) - C_5 s^4 \rho^* A^* \omega^2 W * \bar{g}_s^1(u) = -\tilde{K}^* s^4 g_s^1(u-\xi) \tag{14}$$

where the asterisk in superscript means that the labeled quantity is unknown beforehand. Note that, because of the involvement of unknown material properties and geometric parameters, $\tilde{K}^*$ is not known either, reflected by its superscript.

Equation (14) can be re-arranged as

$$W * \bar{g}_s^5(u) - \frac{C_5 s^4 \rho^* A^* \omega^2}{E^* I^*} W * \bar{g}_s^1(u) = \frac{-\tilde{K}^*}{E^* I^*} s^4 g_s^1(u-\xi), \tag{15}$$

Author's personal copy

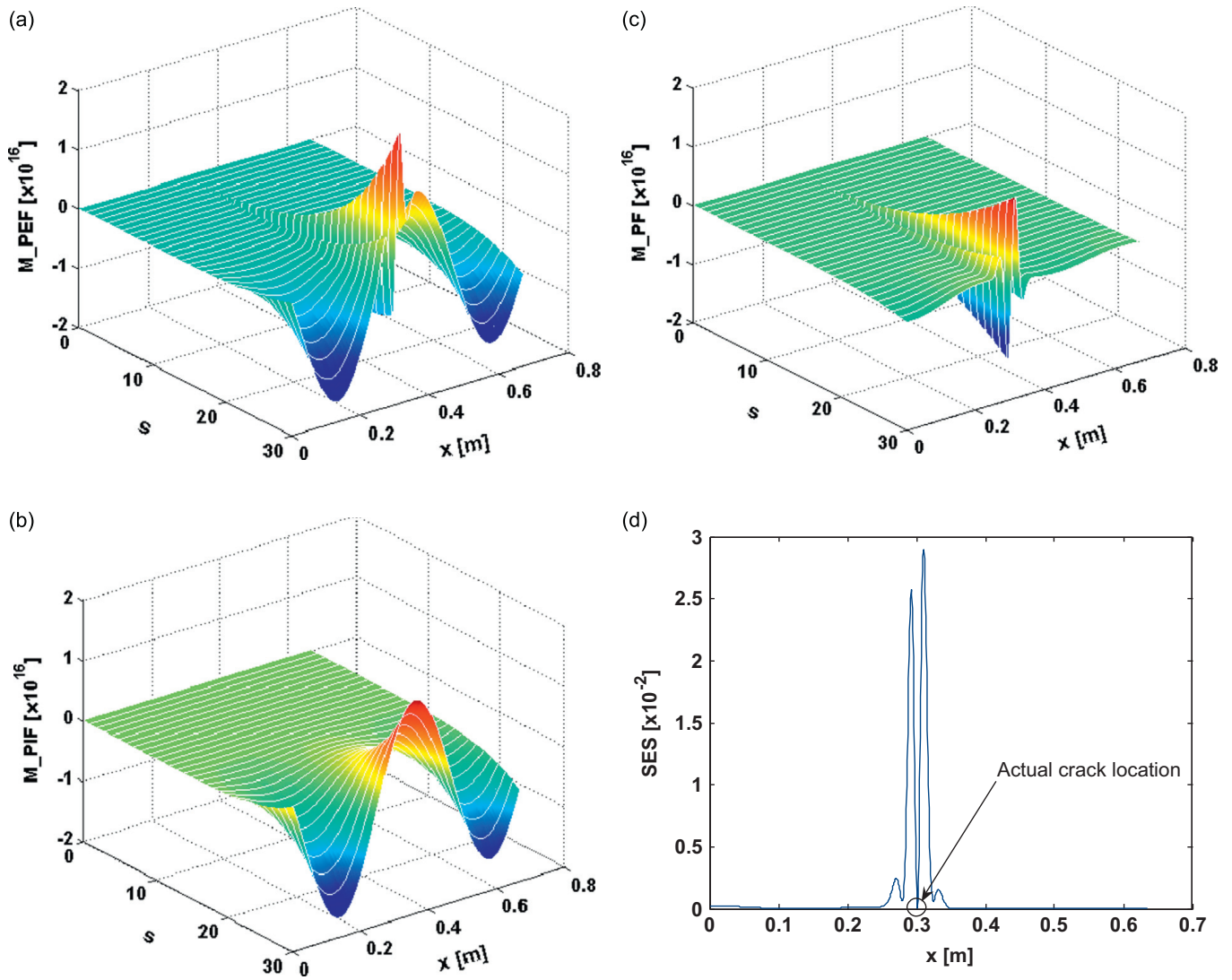

Fig. 2. Graphical representation of the MPDM for an EBC with a crack: (a) *M*_PEF; (b) *M*_PIF; (c) *M*_PF; and (d) SES diagram.

or further simplified by letting $\lambda^*=(\rho^*A^*/E^*I^*)$ and $\gamma^*=(\tilde{K}^*/E^*I^*)$ as

$$W*\bar{g}_s^5(u)-\lambda^*[C_5\omega^2 s^4 W*\bar{g}_s^1(u)]=-\gamma^* s^4 g_s^1(u-\xi) \tag{16}$$

In a concise form, the MPDM becomes

$$\overline{M\_\mathrm{PEF}}-\lambda^*\overline{M\_\mathrm{PIF}}=\gamma^*\overline{M\_\mathrm{PF}}, \tag{17a}$$

where

$$\begin{cases}\overline{M\_\mathrm{PEF}}=W*\bar{g}_s^5(u)\\ \overline{M\_\mathrm{PIF}}=C_5\omega^2 s^4 W*\bar{g}_s^1(u)\\ \overline{M\_\mathrm{PF}}=-s^4 g_s^1(u-\xi).\end{cases} \tag{17b}$$

$\overline{M\_\mathrm{PF}}$ represents the deployment of a series of $-s^4$-modulated Gaussian wavelet $-g^1$ spanning a multi-scale range over the wavelet domain and centered at $u=\xi$. In Eq. (17), provided that λ^*, a combined parameter packaging the material properties and geometric parameters together, can be someway obtained, the acquisition of individual material and geometric parameters will be avoided.

3.2. Multi-scale optimization for estimating λ^*

3.2.1. Zero-integral property of $\overline{M\_\mathrm{PF}}$

Owing to a basic property of the wavelet transform [41]

$$\int g^1(x)\mathrm{d}x=0 \tag{18a}$$

Author's personal copy

the integral of $\overline{M\_\mathrm{PF}}$ (*i.e.*, $-s^4 g_s^1(u-\xi)$) with regard to u, at a given scale s, is

$$\int [-s^4 g_s^1(u-\xi)]\mathrm{d}u = -s^4 \int g_s^1(u-\xi)\mathrm{d}u = 0, \tag{18b}$$

and further, in terms of Eq. (17b), it has

$$\int \gamma^* \overline{M\_\mathrm{PF}}\ \mathrm{d}u = 0. \tag{18c}$$

The property described by Eq. (18c) is called *zero-integral property*. Substituting Eq. (18c) into Eq. (17a) yields

$$\int (\overline{M\_\mathrm{PEF}} - \lambda^* \overline{M\_\mathrm{PIF}})\mathrm{d}u = \int \{W * \bar{g}_s^5(u) - \lambda^* [C_5 \omega^2 s^4 W * \bar{g}_s^1(u)]\}\mathrm{d}u = 0 \tag{19}$$

Benefiting from the zero-integral property, γ^* can be tactically eliminated in Eqs. (18) and (19), while leaving λ^* as the sole parameter to be optimized. The issue of multi-parameter optimization can therefore be degraded to a simple issue concerning mono-parameter optimization, which could be tackled using various general optimization methods. Considering the possible effects of ambient noise and boundary abnormalities. In this study, λ^* in Eq. (19) was ascertained using a mono-parameter optimization approach described as follows (*mono-scale* optimization and *multi-scale* optimization).

3.2.2. Mono-scale optimization

Equation (19) is strictly tenable if exact material and geometric parameters are fed (leading to an exact λ^*). It is however not the case for an estimated λ^* with unknown material and geometric parameters. On that account, Eq. (19) is not expected to be exactly zero, even without the interference from measurement noise and uncertainties. Thus, re-define Eq. (19) in a strict form as

$$\int (\overline{M\_\mathrm{PEF}} - \lambda^* \overline{M\_\mathrm{PIF}})\mathrm{d}u = \int \{W * \bar{g}_s^5(u) - \lambda^* [C_5 \omega^2 s^4 W * \bar{g}_s^1(u)]\}\mathrm{d}u = \varepsilon_s, \tag{20}$$

where ε_s is a deviation from zero due to an inexact λ^* in the equation. Eq. (20) unravels that, provided W and ω are available, ε_s is only subject to λ^*; and therefore a smaller value of ε_s^2 (ε_s can be positive or negative, so ε_s^2 was used to ensure a positive value) corresponds to a more accurate λ^* which is closer to its exact value.

Starting from this point, estimate of λ^* becomes an optimization problem by seeking the minimum of ε_s^2, which can be mathematically defined as

$$\min_{\lambda^*} y_s(\lambda^*) = \min_{\lambda^*}\{\varepsilon_s^2\} = \min \left\{ \int [W * \bar{g}_s^5(u) - \lambda^* C_5 \omega^2 s^4 W * \bar{g}_s^1(u)]\mathrm{d}u \right\}^2, \tag{21a}$$

with an objective function

$$y_s(\lambda^*) = \left\{ \int [W * \bar{g}_s^5(u) - \lambda^* C_5 \omega^2 s^4 W * \bar{g}_s^1(u)]\mathrm{d}u \right\}^2. \tag{21b}$$

Mathematically, Eq. (21) is executed at a single scale s only, accordingly called *mono-scale optimization* hereinafter. The classical N-M simplex algorithm [42] can be employed to solve this optimization problem, inheriting its merits including derivatives-free, quick convergence and easy coding.

3.2.3. Multi-scale optimization

The above mono-scale optimization is expected to be effective for an ideal scenario in which the measurement is free of measurement noise. Nevertheless, an experimentally captured $W(x)$ is unavoidably contaminated by measurement noise and uncertainties. In addition, numerical abnormities incurred from convolution in the model ($W * \bar{g}_s^5(u)$ and $W * \bar{g}_s^1(u)$) may become remarkable in the adjacent regions around $W(0)$ and $W(l)$ (*i.e.*, both ends of the EBC). The measurement noise, uncertainties and numerical abnormities, varying as scale s, can jointly add errors to ε_s^2, making it somewhat troublesome to select a favorable scale at which the mono-scale optimization can be efficiently implemented so as to reach an optimal λ^*.

Practically, it may be a challenge to determine a particular scale at which the mono-scale optimization is applied. Thus a mono-scale optimization is executed at multiple scales. A series of mono-scale optimization, defined by Eq. (20) at individual scales, is performed independently at every single scale within a scale range of interest, leading to a sequence of ε_s^2. Amongst all ε_s^2, those with lower magnitudes and more stable variation imply that, at those scales, the damage-associated signal features play a dominant role, overwhelming random measurement noise/uncertainties and numerical abnormities from convolution. Therefore these ε_s^2 contribute to an optimal λ^* closer to its exact value. For convenience of discussion, the scalar fragment containing such ε_s^2 of lower magnitudes and more stable variation is referred to as *effective scale interval*, represented by $[s_p, s_q]$. Combining all the mono-scale optimization at every single scale over $[s_p, s_q]$ forms a *multi-scale optimization* of λ^*, defined as

$$\min_{\lambda^*} y_{[s_p,s_q]}(\lambda^*) = \min_{\lambda^*} \int_{s_p}^{s_q} \left\{ \int [W * \bar{g}_s^5(u) - \lambda^* C_5 \omega^2 s^4 W * \bar{g}_s^1(u)]\mathrm{d}u \right\}^2 \mathrm{d}s, \tag{22a}$$

Author's personal copy

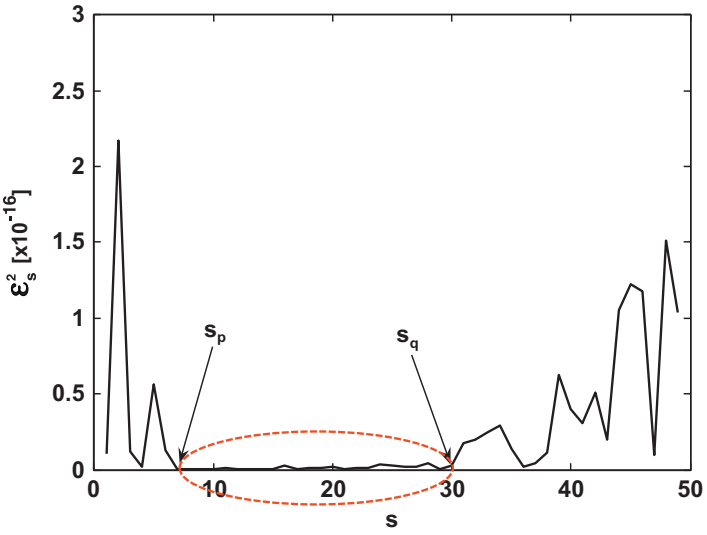

Fig. 3. Illustration of selecting effective scale interval $[s_p, s_q]$.

with an objective function of

$$y_{[s_p,s_q]}(\lambda^*) = \int_{s_p}^{s_q} \left\{ \int [W * \bar{g}_s^5(u) - \lambda^* C_5 \omega^2 s^4 W * \bar{g}_s^1(u)] \mathrm{d}u \right\}^2 \mathrm{d}s \tag{22b}$$

where $s \in [s_p, s_q]$. Eq. (22) is an expansion of Eq. (20) from a mono-scale to a multi-scale, reflecting more dynamics features of the EBC under practical measurement condition with noise interference and uncertainties. Essentially, the multi-scale optimization is a series of statistically consolidated mono-scale optimization, whereby λ^* can be ascertained more accurately in noisy measurement conditions.

By way of illustration, Fig. 3 exemplarily presents a series of ε_s^2 in an interested range of scale, including an effective scale interval $[s_p, s_q]$, within which ε_s^2 are small compared with those falling out $[s_p, s_q]$. Those ε_s^2 at scales greater than s_q (*viz.*, lower frequencies) with much higher amplitude can be attributed to the abnormities from numerical convolution; while ε_s^2 at scales less than s_p (*viz.*, higher frequencies) are due to random measurement noise.

3.3. Damage identification using multi-scale optimization

Capitalizing on the above multi-scale optimization, a damage identification strategy, tolerating the absence of knowledge on material properties, geometric features and boundary conditions, was developed.

Re-define the MPDM described by Eq. (16) as

$$W * \bar{g}_s^5(u) - \hat{\lambda}^* [C_5 \omega^2 s^4 W * \bar{g}_s^1(u)] = -\gamma^* s^4 \widehat{g_s^1}(u - \xi) \tag{23a}$$

or in a concise form as

$$(\overline{M\_\mathrm{PEF}} - \hat{\lambda}^* \overline{M\_\mathrm{PIF}}) = \gamma^* \widehat{\overline{M\_\mathrm{PF}}} \tag{23b}$$

where $\hat{\lambda}^*$ denotes an optimal λ^* estimated using Eq. (22). Substituting $\hat{\lambda}^*$ into the left-hand-side term of Eq. (23b) yields $\gamma^* \widehat{\overline{M\_\mathrm{PF}}}$ at the current $\hat{\lambda}^*$. Further, the damage in the EBC causes drastic change in $\gamma^* \widehat{\overline{M\_\mathrm{PF}}}$ at the location where the damage exists (ξ). In virtue of SES defined by Eq. (13), SES of $\gamma^* \widehat{\overline{M\_\mathrm{PF}}}$ over $[s_p, s_q]$, is specified by

$$\mathrm{SES}(u) = \frac{\int_{s_p}^{s_q} \left(\gamma^* \widehat{\overline{M\_\mathrm{PF}}} \right)^2 \mathrm{d}s}{\int_{s_p}^{s_q} \int_0^l \left(\gamma^* \widehat{\overline{M\_\mathrm{PF}}} \right)^2 \mathrm{d}u \, \mathrm{d}s} \tag{24}$$

SES of $\gamma^* \widehat{\overline{M\_\mathrm{PF}}}$ in Eq. (24) (note: neither material nor geometric parameters are requested) has the same physical significance for characterizing a crack as the SES of $M_$PF in Eq. (13). But the latter demands explicitly defined material and geometric parameters beforehand.

Author's personal copy

4. Proof-of-concept validation using numerical simulation

Feasibility of the proposed damage identification strategy was first examined using finite element (FE) simulations.

4.1. Modeling

Consider an EBC (l=0.63 m) as shown in Fig. 4, the shadowed part of a simply-supported steel system (E_0=206 GPa; ρ_0=7800 kg/m^3; L=1 m). The system had unknown boundary conditions, represented by two rotational springs, R_1 and R_2, and two tensional springs, T_1 and T_2, at each end. The EBC was assumed to contain a double-edged crack at ξ=0.3 m. A dimensionless parameter $\beta=2e/h$ was introduced to define the crack severity, where $2e$ is the total reduction in the depth committed by the crack (e for each side). The entire system was subject to a transverse mono-frequency excitation, $F_0\delta(x+d)e^{i\omega t}$, 0.08 m from the origin (d=−0.08 m, F_0=1000 kN). Different frequencies (ω), as listed in Table 1, were comparatively selected for excitation.

The entire system was simulated using *ca.* 1450 Euler–Bernoulli beam elements, with the crack modeled using a specific crack element featuring a reduced size in its depth. The use of Euler–Bernoulli beam elements was aimed at matching the previous analytical modeling in which the one-dimensional beam equilibrium equation for Euler–Bernoulli beam was used. The modal superposition method [7] was employed to solve the system equation. Letting $\mathbf{W}^i_*(\omega_i)$ be the ith-order mode shape vector of the structure, and ω_i the corresponding modal frequencies, the transverse displacement of the structure at an arbitrary frequency ω, $\mathbf{W}^*(\omega)$, can be expressed as [7]

$$\mathbf{W}_*(\omega)=\sum_i \frac{\mathbf{W}^i_*(\omega_i)[\mathbf{W}^i_*(\omega_i)\mathbf{F}]}{\omega_i^2-\omega^2}, \tag{25}$$

where $\mathbf{F}$ is the magnitude vector of excitation force applied to the structure (non-zero at and only at $x=-d$). With the calculated $\mathbf{W}^*(\omega)$, the transverse displacement vector of the EBC, $\mathbf{W}(\omega)$, was obtained, which corresponded to $W(x)$ requested in the MPDM.

The aforementioned multi-scale optimization provides certain flexibility in selecting the excitation frequency within a wide range. In this study, three levels of crack severity (severity I, II, and III, via changing e in $\beta=2e/h$) at three excitation frequencies ($\omega_{\mathbf{I}}$, $\omega_{\mathbf{II}}$ and $\omega_{\mathbf{III}}$) (see Table 1) are examined, respectively. $\omega_{\mathbf{I}}$, $\omega_{\mathbf{II}}$ and $\omega_{\mathbf{III}}$ are arbitrarily chosen between two neighboring resonance frequencies of the system (for reference, the calculated neighboring resonance frequencies of the system for $\omega_{\mathbf{I}}$, $\omega_{\mathbf{II}}$ and $\omega_{\mathbf{III}}$, respectively, are also given in Table 1). Up to eight signal-to-noise ratios (SNRs) were considered (SNR=∞, 120, 100, 90, 80, 70, 60 and 50 dB). Combination of the above three damage severities and eight SNRs led to 24 damage scenarios. $\mathbf{W}(\omega)$ for each scenario was obtained, as shown in Fig. 5 for three examples (three damage severities in the absence of measurement noise (when SNR=∞)), from which no any information associated with the damage can be captured.

4.2. Validation

In what follows, material properties, geometric parameters and boundary conditions were assumed to be unknown *a priori*.

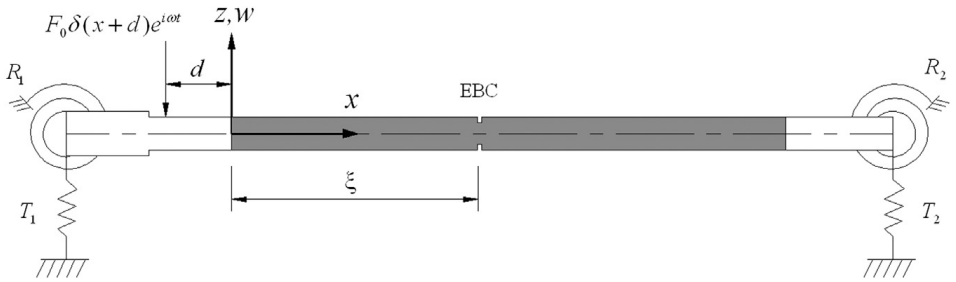

Fig. 4. An EBC bearing a double-edged crack, as a part of a structural system with indeterminate boundary conditions.

Table 1
Damage cases used in simulation (ξ=0.3 m).

Damage severity	Crack depth ratio (β)	Excitation frequency (ω [Hz])	Modal frequency immediately before ω (ω_i [Hz])	Modal frequency immediately after ω (ω_j [Hz])
I	0.1	$\omega_{\mathbf{I}}$=1453	ω_4=1134	ω_5=1787
II	0.2	$\omega_{\mathbf{II}}$=2105	ω_5=1786	ω_6=2596
III	0.3	$\omega_{\mathbf{III}}$=5080	ω_8=4682	ω_9=5950

Author's personal copy

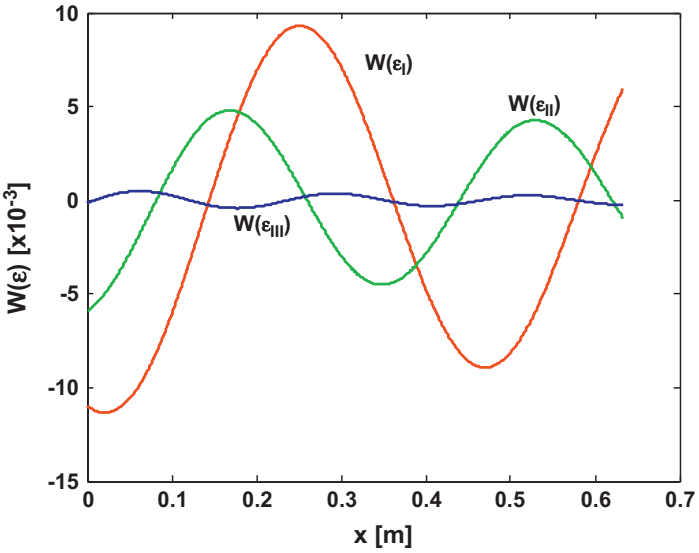

Fig. 5. $W(x)$ of the EBC shown in Fig. 4 with three crack severities in the absence of measurement noise (when SNR$=\infty$).

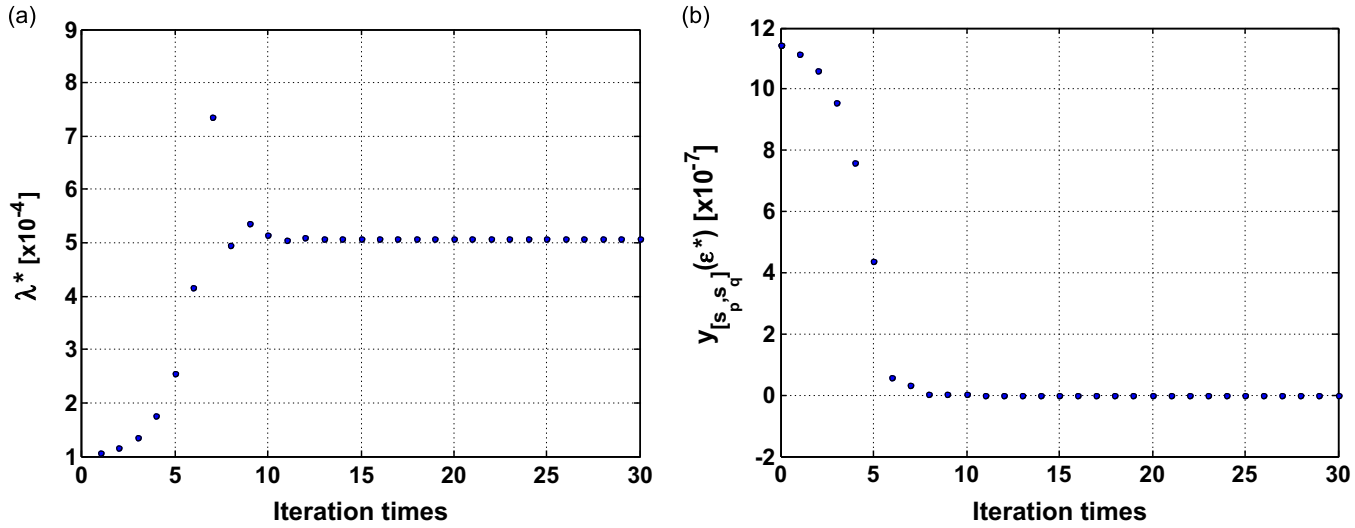

Fig. 6. Progressive convergence of optimization for (a) λ^* and (b) $y_{[s_p,s_q]}(\lambda^*)$.

Randomly, damage severity I when SNR$=$120 dB was first selected for validation. The effective scale interval for this case was determined to be $[s_7, s_{30}]$ ($s_p=7$ and $s_q=30$), as shown in Fig. 3, according to the criteria afore-addressed in Section 3.2.3.

Applying Eq. (22) and using the N-M simplex algorithm, Fig. 6(a) and (b) display, respectively, the progressive convergence of the optimization for estimating λ^* and $y_{[s_p,s_q]}(\lambda^*)$, to observe that λ^* converged and stabilized after *ca.* 10 iterations, at which $\widehat{\lambda^*} = 5.0617 \times 10^{-4}$.

The obtained $\widehat{\lambda^*}$ was then substituted into the MPDM defined by Eq. (23), to quantify the crack. Three terms of the MPDM (*i.e.*, $\overline{M\_\mathrm{PEF}}$, $\widehat{\lambda^*}\overline{M\_\mathrm{PIF}}$ and $\gamma^*\widehat{\overline{M\_\mathrm{PF}}}$) are shown in Fig. 7(a–c), respectively. In Fig. 7(c), $\gamma^*\widehat{\overline{M\_\mathrm{PF}}}$ clearly highlights the damage features in conformity to the pattern of $-s^4$-modulated $g_s^1(u-\xi)$. To better visualize the damage location, the corresponding SES diagram is presented in Fig. 7(d), in which the trough between a pair of prominent peaks indicates the estimated location of the damage, well matching the reality ($\xi=0.3$ m).

It is interesting to compare the results shown in Fig. 2 with Fig. 7. The former arose from a forward analysis with known material properties, geometric parameters and boundary conditions of the EBC; while the latter from a backward analysis with $\mathbf{W}(\omega)$ being the only prerequisite. The quantitative agreement between the two sets of results demonstrated that the proposed damage characterization strategy is able to quantify damage with satisfactory accuracy and precision, even without prior knowledge on these basic parameters.

Author's personal copy

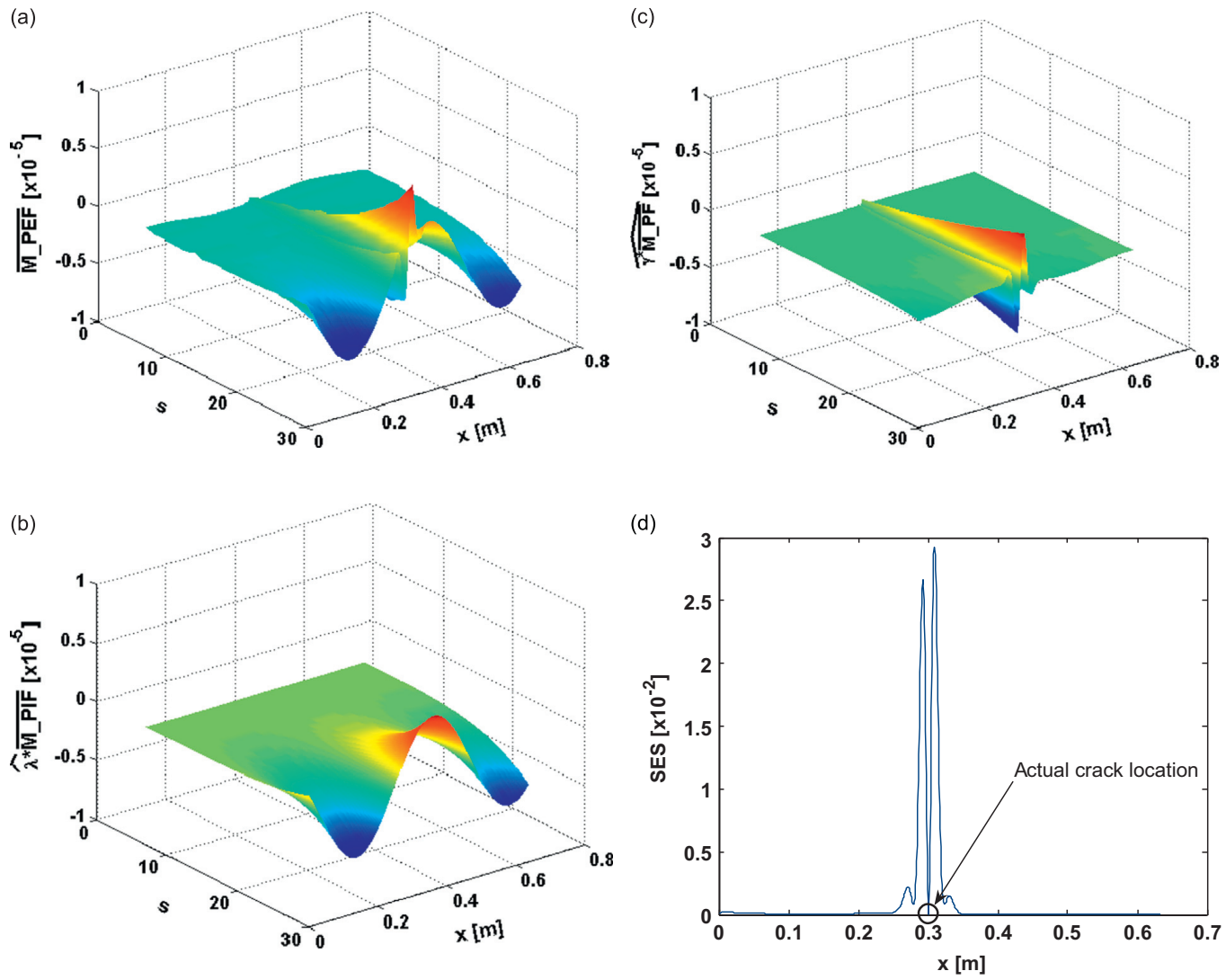

Fig. 7. MPDM-based characterization results (for severity I when SNR=120 dB) with unbeknown material/geometric properties and boundary conditions: (a) $\overline{M}\_\mathrm{PEF}$; (b) $\lambda^*\overline{M}\_\mathrm{PIF}$; (c) $\gamma^*\overline{M}\_\mathrm{PF}$; and (d) SES diagram.

4.3. Parametric studies and discussion

4.3.1. Robustness to measurement noise

Robustness of the proposed characterization strategy under noisy measurement conditions was examined using the 24 damage scenarios, with different levels of SNR added to the calculated $\mathbf{W}(\omega)$. The same optimization procedure was employed to obtain $\widehat{\lambda^*}$. As some typical results for the slightest damage (severity I ($\beta=0.1$)), Table 2 lists the estimated $\widehat{\lambda^*}$ at different levels of SNR ranging from ∞ to 50 dB. It can be seen that with a decrease in SNR (severer noise), the estimated $\widehat{\lambda^*}$ gradually deviates from that ascertained when SNR$=\infty$ (the case without any interference from measurement noise). The SES diagrams for three arbitrarily selected scenarios when SNR=75, 70 and 65 dB, respectively, are shown in Fig. 8 for comparison. It can be seen that the proposed strategy can identify a fine crack ($\beta=0.1$) under the influence of measurement noise with a SNR over 70 dB. For a severer crack (severity II ($\beta=0.2$) or III ($\beta=0.3$)), the tolerance to noise can be even better, as demonstrated in Fig. 9, in which the crack location can be recognized for severity II when SNR=60 dB, and for severity III when SNR=50 dB. The multi-scale nature of the optimization defined by Eq. (22) empowers the approach with enhanced robustness under noisy measurement conditions.

4.3.2. Flexibility in selection of effective scale intervals

As commented previously, the effective scale interval enables a multi-scale optimization for estimating λ^* with enhanced accuracy and reliability. Even when the selected interval is just a sub-interval of the full effective scale interval, the accuracy and precision of the strategy would not be impaired phenomenally. Using a damage scenario (severity I when SNR=120) as an example, Table 3 lists the estimated λ^* using sub-intervals, to observe that all the estimated λ^* are still very close to that when the full interval $[s_7, s_{30}]$ was used. Such a trait renders twofold advantages to the MPDM: (i) appreciable tolerance to

Author's personal copy

Table 2
Estimated $\widehat{\lambda}^*$ under different levels of SNR using *effective scale interval* in multi-scale optimization.

SNR	∞	120	100	90	80	70	60	50
$\widehat{\lambda}^*$ [$\times 10^{-4}$]	5.0437	5.0617	5.1031	5.1439	5.1664	5.2374	5.64219	6.1729

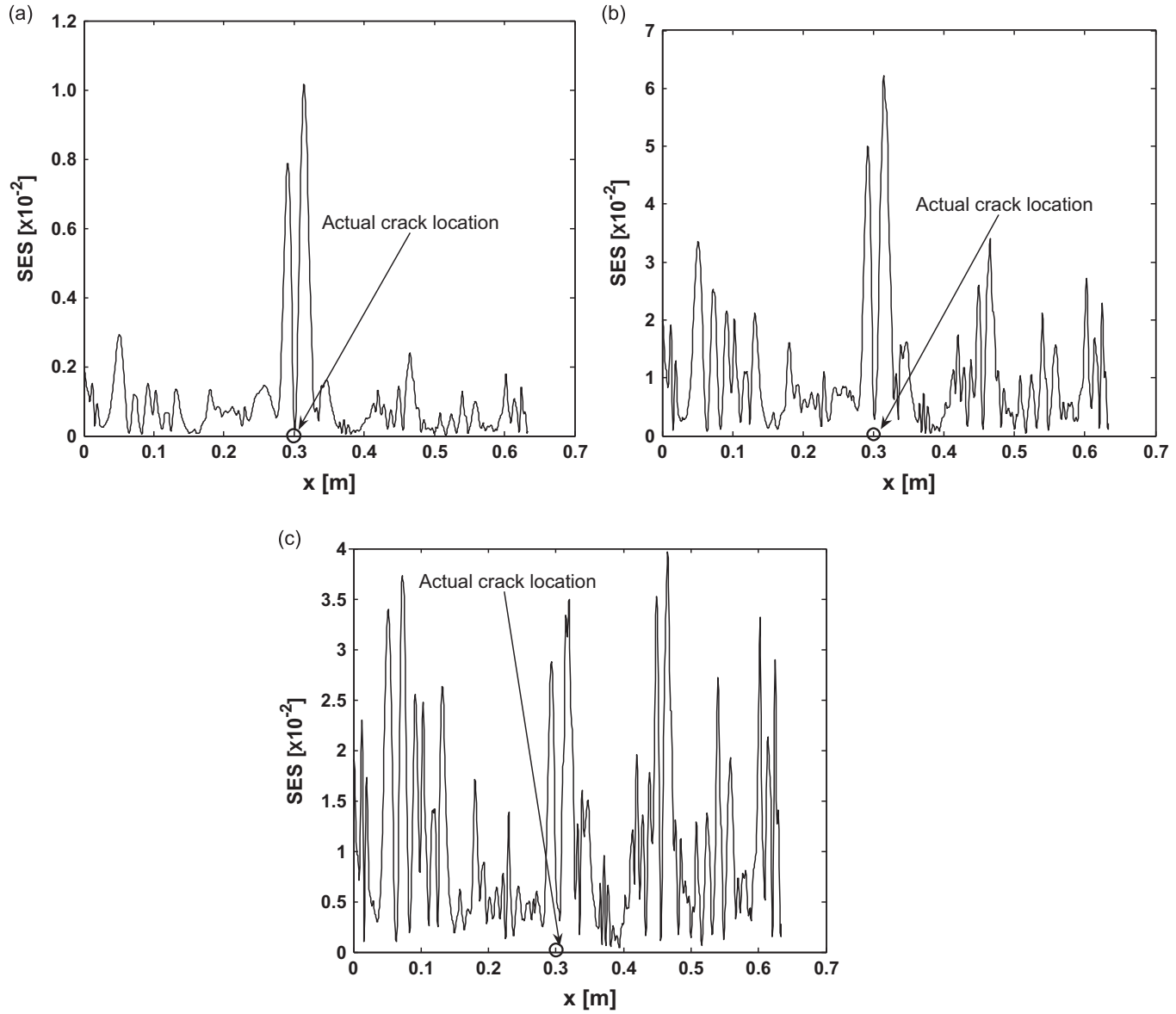

Fig. 8. Capacity of noise tolerance of MPDM-based characterization (for severity I) when (a) SNR=75; (b) SNR=70; and (c) SNR=65.

errors during selection of an effective scale interval; and (ii) reduction in calculation cost. Such a flexibility of the approach in turn corroborates the vigorousness of the model.

4.3.3. Superiority over traditional methods

To evaluate the performance of the proposed strategy against traditional curvature-based and CWT-based methods mentioned previously, the three detection methods were respectively employed to characterize two arbitrarily selected damage cases (severity II (β=0.2) when SNR=65 dB; severity III (β=0.3) when SNR=55 dB). The characterization results are shown in Figs. 10–12, respectively for three approaches. In Fig. 10, the curvatures of $W(x)$ are unable to predict either of the two scenarios due to the considerable interference from high-frequency measurement noise. In Fig. 11, the wavelet

Author's personal copy

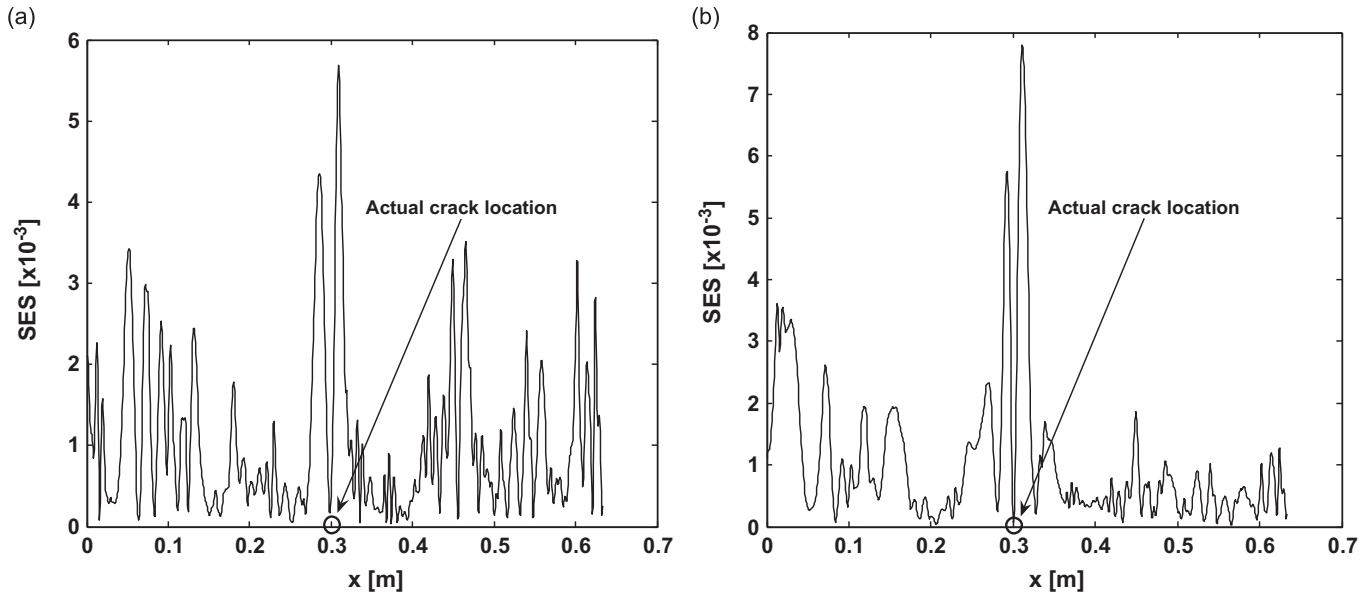

Fig. 9. Capacity of noise tolerance of MPDM-based characterization for (a) severity II when SNR=60 dB; and (b) severity III when SNR=50 dB.

Table 3
Estimated $\widehat{\lambda^*}$ using *sub-intervals* in multi-scale optimization (SNR=120).

Sub-interval	$[s_{25}, s_{30}]$	$[s_{20}, s_{25}]$	$[s_{15}, s_{20}]$	$[s_{17}, s_{18}]$
$\widehat{\lambda^*}[\times 10^{-4}]$	5.0675	5.0366	5.0490	5.0764

Note: Full effective scale interval: $[s_7, s_{30}]$; corresponding $\widehat{\lambda^*}$: 5.0617×10^{-4}.

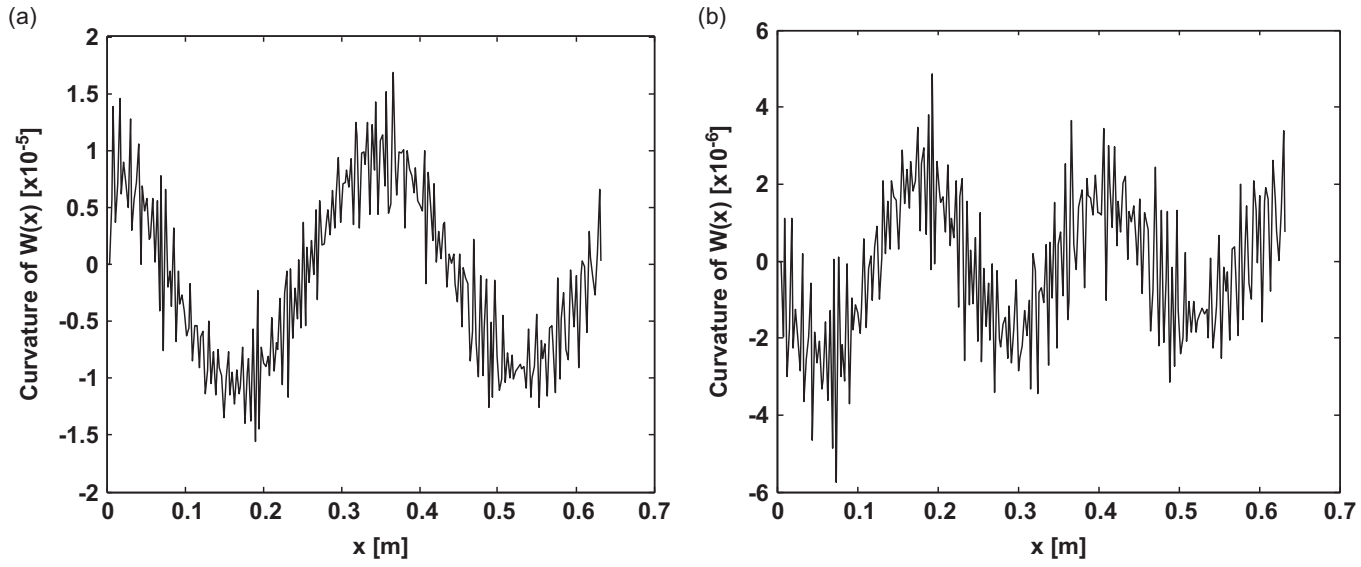

Fig. 10. Characterization results using curvature-based method for (a) severity II when SNR=65 dB; and (b) severity III when SNR=55 dB.

scalograms of $W(x)$ (using g^5 as the mother wavelet, the same as that used in the MPDM) fails to locate the damage exactly either, as a result of the influence arising from the low-frequency trend component in $W(x)$ (a captured $W(x)$ manifests collective contributions from both a trend component in a lower-frequency band and a crack-induced local perturbation in a higher-frequency band [38]). In contrast, using the proposed approach, the MPDM in Fig. 12 exactly points out the crack

Author's personal copy

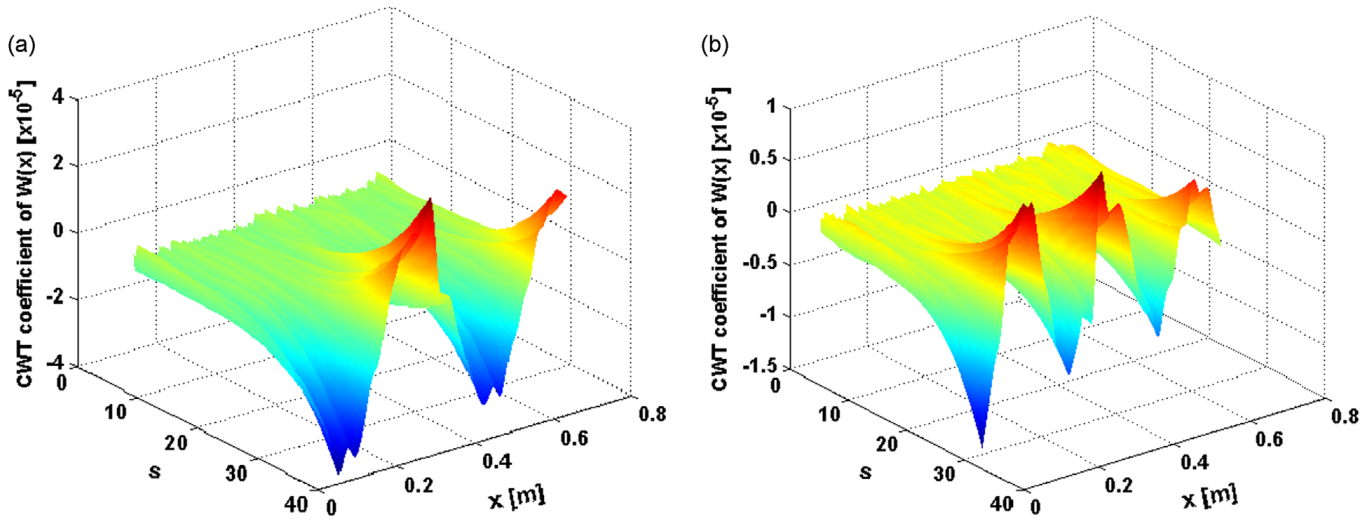

Fig. 11. Characterization results using CWT-based method for (a) severity II when SNR=65 dB; and (b) severity III when SNR=55 dB.

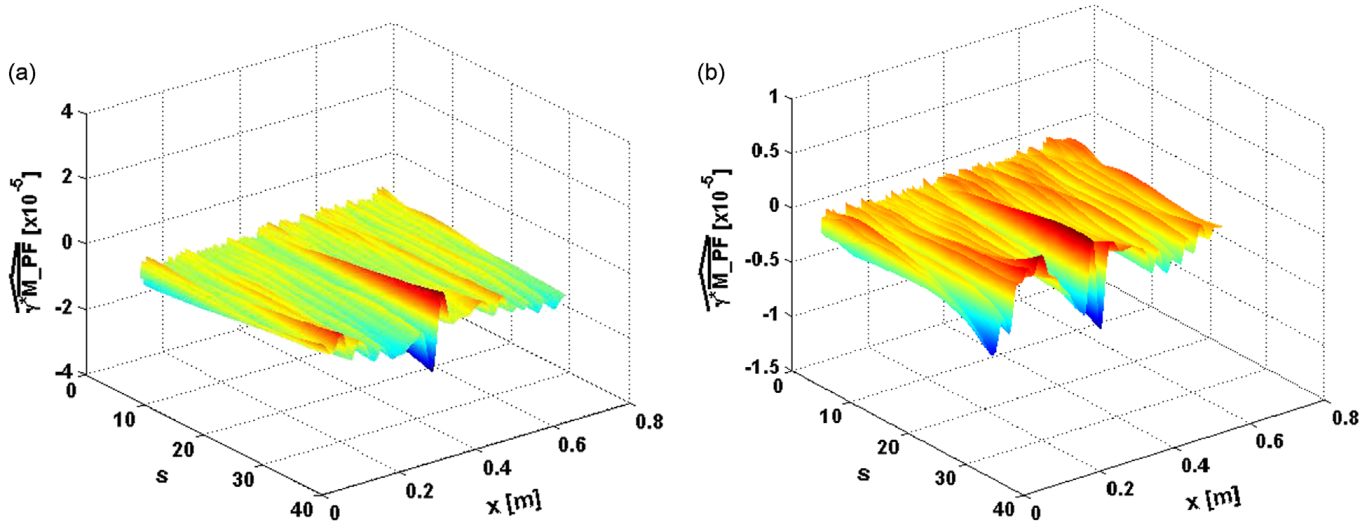

Fig. 12. Characterization results using MPDM-based method for (a) severity II when SNR=65 dB; and (b) severity III when SNR=55 dB.

location. These results can be better understood in their corresponding SES diagrams in Fig. 13. Based on the above comparison, conclusion can thus be drawn that the proposed method outperforms two major existing approaches.

5. Experimental validation

Effectiveness of the proposed damage characterization strategy was validated experimentally using a scanning laser vibrometer (SLV). A structure containing an EBC fragment was prepared, shown in Fig. 14, assuming that the density and modulus of elasticity of the EBC were unbeknown *a priori*. To demonstrate the independence of modeling of structural boundary, the system was deliberately designed to feature irregular boundaries: one end being fixed and the other being free with an irregular shape, with all dimensions indicated in the figure. A through-width crack, 1.2 mm long along the beam span and 2 mm deep, was introduced to the EBC, 220 mm from the clamped end. An electromechanical shaker (B&K® 4809) was used to generate an out-of-plane (*z*-direction) mono-frequency excitation at 2 kHz at the location 25 mm from the free end edge. Such an excitation frequency was selected in accordance with a spectrum analysis. The out-of-plane velocities at all the measurement points along the central line of the beam (evenly distributed with a spacing interval of 2.6 mm) was captured with an SLV (Polytec® PSV-400), which were then integrated to the out-of-plane displacement responses (*i.e.*, $\mathbf{W}(\omega)$) using a FAST-SCAN function. Note that the velocity was acquired from the intact surface of the beam, opposite to which lay the damage. The experiment setup is photographed in Fig. 15.

Fig. 16 presents progressive convergence of the multi-scale optimization, to see that λ^* converged and stabilized after *ca.* 12 iterations, at which $\widehat{\lambda^*} = 7.3218 \times 10^{-3}$. The established MPDM is shown in Fig. 17(a–c) for $\overline{M\_\mathrm{PEF}}$, $\widehat{\lambda^*}\overline{M\_\mathrm{PIF}}$ and $\gamma^*\overline{M\_\mathrm{PF}}$,

Author's personal copy

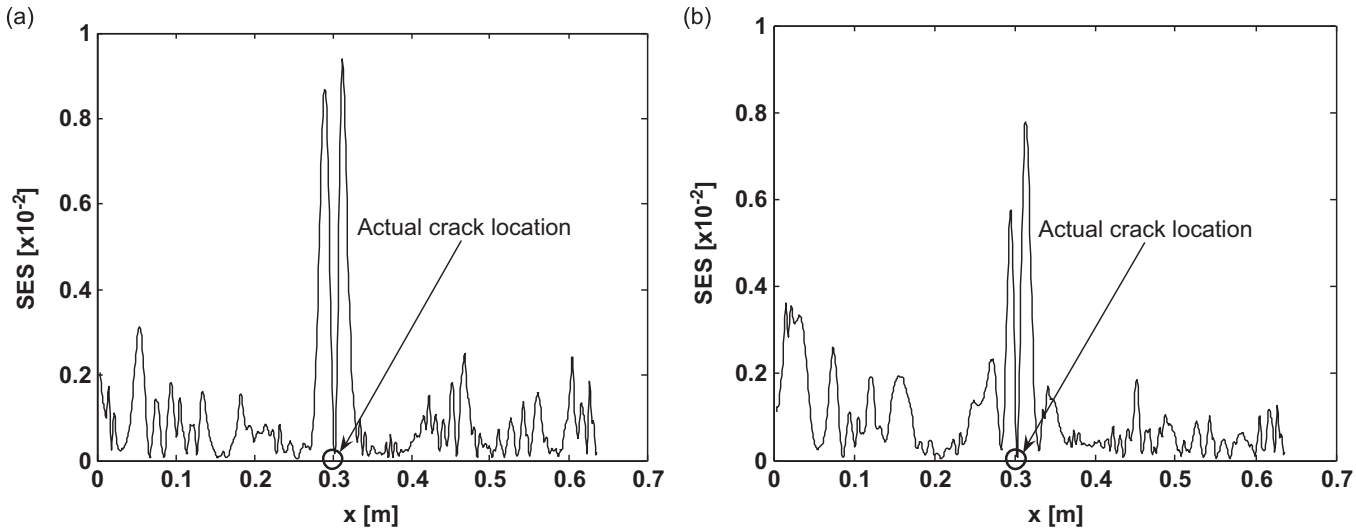

Fig. 13. SES diagrams of the MPDM for (a) severity II when SNR=65 dB; and (b) severity III when SNR=55 dB.

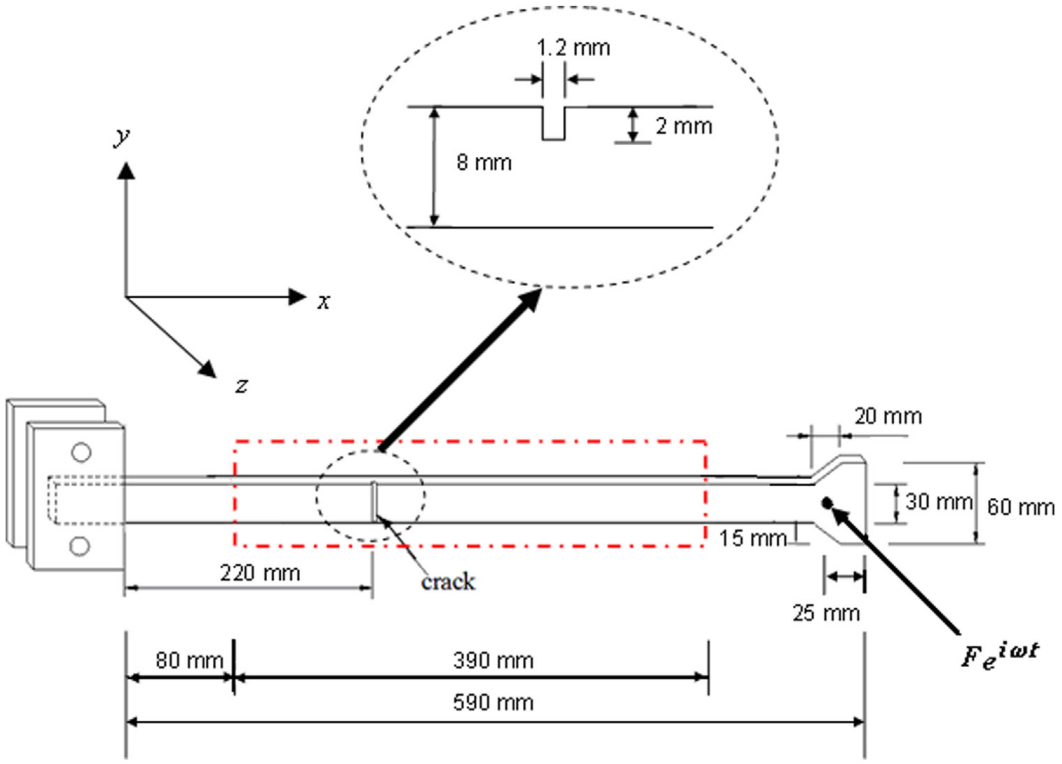

Fig. 14. A structural system with irregular boundaries, containing an EBC with a through-width crack, for experimental validation.

respectively, and the corresponding SES diagram in Fig. 17(d) upon determination of the effective scale interval for this case being $[s_1, s_{10}]$. In Fig. 17(c) and (d), singularity due to the damage protrudes, noticeably highlighting the crack location (223 mm from the clamped end), well matching the reality (220 mm).

6. Concluding remarks

A quantitative damage characterization strategy was established based on a multi-scale pseudo-force damage model over a wavelet domain, which is empowered with the capability of tolerating the absence of prior knowledge on partial material properties and structural parameters. Such an attribute of the approach allows robust damage characterization in engineering practice in which it may be somewhat difficult or even impossible to acquire those prerequisite parameters

Author's personal copy

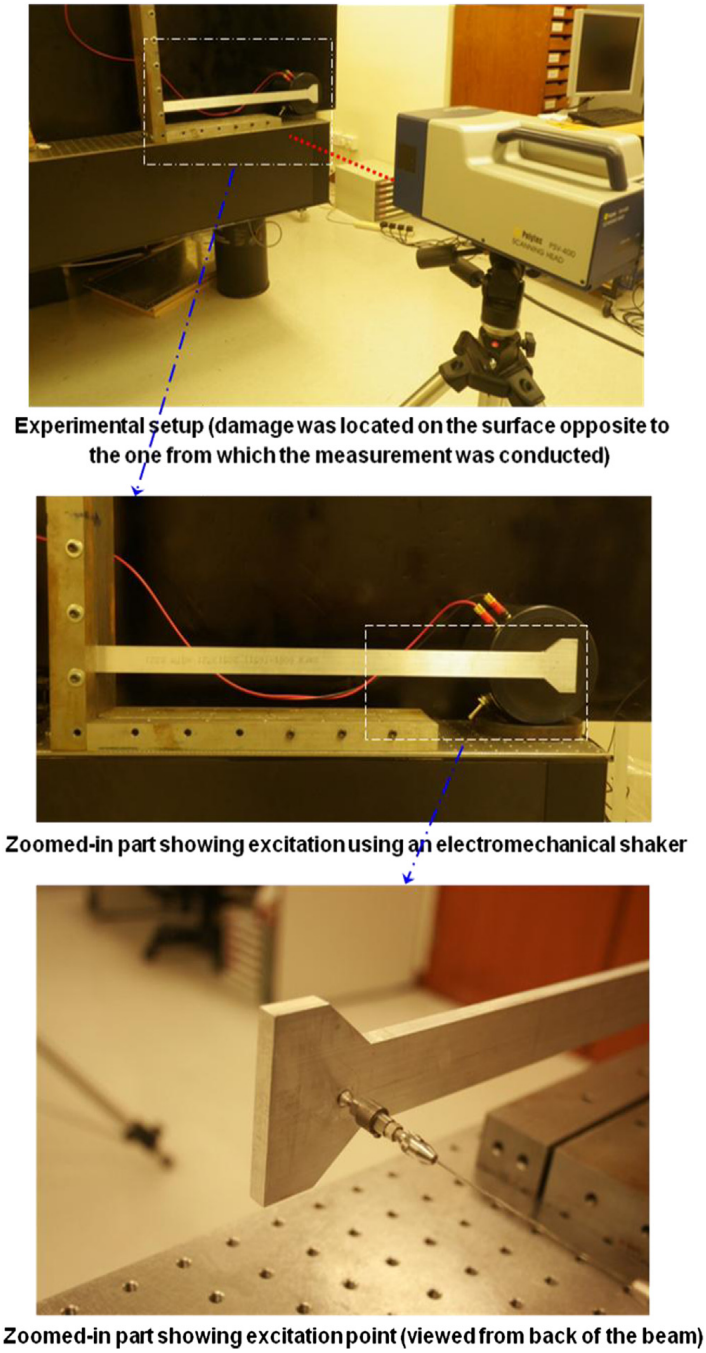

Fig. 15. Experimental setup for acquiring $W(x)$ with an SLV from the intact beam surface (*i.e.*, the surface opposite to which lay the damage).

beforehand. Benefiting from the model which '*locally*' examines perturbance to dynamic characteristics in a point-by-point manner, this strategy is able to bypass major limitations of global vibration-based or local guided-wave-based damage detection: it requires neither benchmark structures nor baseline signals; neither global models nor particular requirement for additional excitation source as long as the structure undergoes steady vibration under its normal operation. Using the approach, characterization of a fine crack in an EBC was conducted in both simulation and experiment without knowing material properties, geometric features and boundary conditions beforehand. Results demonstrated the satisfactory accuracy and robustness of the approach under noisy measurement conditions. Benefiting from the nature of local examination, development philosophy of the model can be extended to different types of structural components such as beam, plate or shell. It is noteworthy that the proposed approach can be vulnerable to measurement noise because of the use of vibration features in the relatively low frequency range. To circumvent possible impact of ambient noise on the accuracy of the approach, mono-scale optimization can be applied as a de-noising treatment. In addition, owing to the local inspection nature, the approach can also be readily extended to the detection of multiple-damage within the same inspection region, showing advantages over conventional global detection methods. Examination of the proposed approach using more complex structures will be carried out in future study.

Author's personal copy

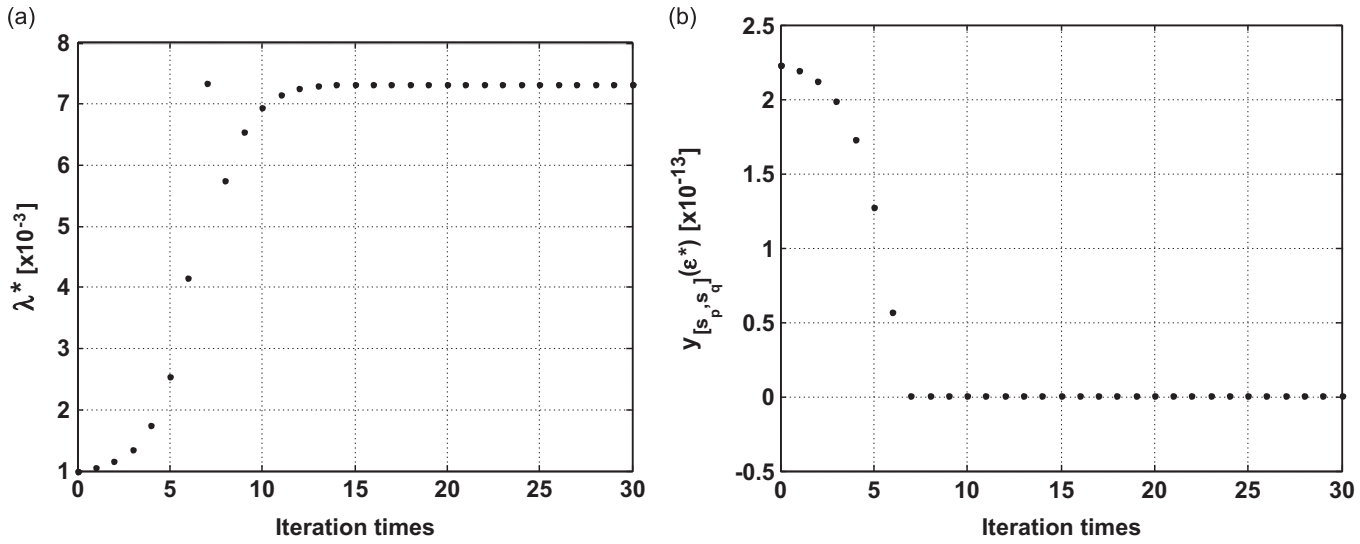

Fig. 16. Progressive convergence of optimization for (a) λ^* and (b) $y_{[s_p,s_q]}(\lambda^*)$.

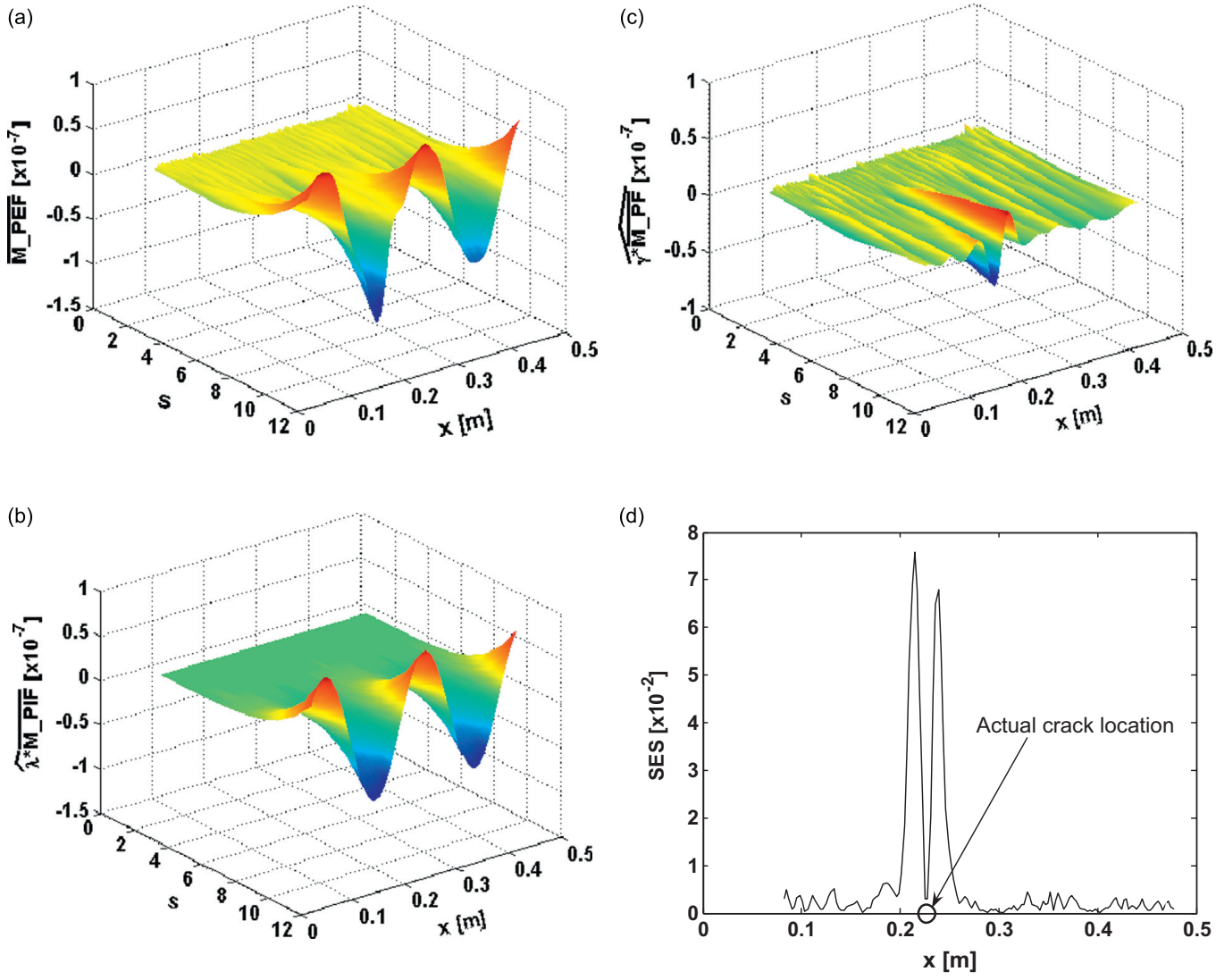

Fig. 17. MPDM-based characterization results for the crack shown in Figs. 14 and 15 with unbeknown material/geometric properties and boundary conditions: (a) $\overline{M\_PEF}$; (b) $\lambda^*\overline{M\_PIF}$; (c) $\gamma^*\widetilde{M\_PF}$; and (d) SES diagram.

Author's personal copy

Acknowledgments

The work described in this paper was supported partially by the National Natural Science Foundations of China (No. 11272272). M. Cao is grateful to National Natural Science Foundations of China for Grant nos. 50978084 and 11172091.

References

[1] Z. Su, L. Ye, *Identification of Damage Using Lamb Waves: From Fundamentals to Applications*, Springer-Verlag, London, 2009.
[2] D.E. Adams, *Health Monitoring of Structural Materials and Components: Methods with Applications*, Wiley, New York, 2007.
[3] J.D. Achenbach, Quantitative nondestructive evaluation, *International Journal of Solids and Structures* 37 (1–2) (2000) 13–27.
[4] C. Boller, Ways and options for aircraft structural health management, *Smart Materials and Structures* 10 (2001) 432–440.
[5] C.R. Farrar, K. Worden, An introduction to structural health monitoring, *Philosophical Transactions of the Royal Society A: Mathematical, Physical and Engineering Sciences* 365 (2007) 303–315.
[6] V. Giurgiutiu, *Structural Health Monitoring with Piezoelectric Wafer Active Sensors*, Elsevier Academic Press, Boston, 2008.
[7] D.J. Inman, *Engineering Vibration*, Prentice Hall, Upper Saddle River, 2000.
[8] P.Z. Qiao, M.S. Cao, Waveform fractal dimension for mode shape-based damage identification of beam-type structures, *International Journal of Solids and Structures* 45 (22–23) (2008) 5946–5961.
[9] H. Sohn, C.R. Farrar, F.M. Hemez, D.D. Shunk, D.W. Stinemates, B.R. Nadler, *A review of structural health monitoring literature: 1996–2001*, , 2003 Los Alamos National Laboratory Report, LA-13976-MS.
[10] W.J. Staszewski, C. Boller, G.R. Tomlinson, *Health Monitoring of Aerospace Structures: Smart Sensor Technologies and Signal Processing*, John Wiley & Sons, Chichester, 2004.
[11] J.L. Wang, P.Z. Qiao, Vibration of beams with arbitrary discontinuities and boundary conditions, *Journal of Sound and Vibration* 308 (1–2) (2007) 12–27.
[12] C.R. Farrar, S.W. Doebling, D.A. Nix, Vibration-based structural damage identification, *Philosophical Transactions of the Royal Society A: Mathematical, Physical and Engineering Sciences* 359 (2001) 131–149.
[13] J.T. Kim, Y.S. Ryu, H.M. Cho, N. Stubbs, Damage identification in beam-type structures: frequency-based methods *vs.* mode shape-based method, *Engineering Structures* 25 (1) (2003) 57–67.
[14] Y. Zou, L. Tong, G.P. Steven, Vibration-based model-dependent damage (delamination) identification and health monitoring for composite structures—a review, *Journal of Sound and Vibration* 230 (2) (2000) 357–378.
[15] J. Chen, Z. Su, L. Cheng, Identification of corrosion damage in submerged structures using fundamental anti-symmetric Lamb waves, *Smart Materials and Structures* 19 (1) (2010) 015004. (12 pp.).
[16] P. Fromme, P.D. Wilcox, M.J.S. Lowe, P. Cawley, On the development and testing of a guided ultrasonic wave array for structural integrity monitoring, *IEEE Transactions on Ultrasonics, Ferroelectrics, and Frequency Control* 53 (2006) 777–785.
[17] V. Giurgiutiu, J. Bao, Embedded-ultrasonics structural radar for *in situ* structural health monitoring of thin-wall structures, *Structural Health Monitoring: An International Journal* 3 (2004) 121–140.
[18] B. Ihn, F.-K. Chang, Pitch-catch active sensing methods in structural health monitoring for aircraft structures, *Structural Health Monitoring: An International Journal* 7 (2008) 5–19.
[19] G. Konstantinidis, B.W. Drinkwater, P.D. Wilcox, The temperature stability of guided wave structural health monitoring systems, *Smart Materials and Structures* 15 (2006) 967–976.
[20] T. Kundu, S. Das, K.V. Jata, Health monitoring of a thermal protection system using Lamb waves, *Structural Health Monitoring: An International Journal* 8 (2009) 29–45.
[21] J.E. Michaels, T.E. Michaels, Guided wave signal processing and image fusion for *in situ* damage localization in plates, *Wave Motion* 44 (2007) 482–492.
[22] W. Ostachowicz, P. Kudela, P. Malinowski, T. Wandowski, Damage localisation in plate-like structures based on PZT sensors, *Mechanical Systems and Signal Processing* 23 (2008) 1805–1829.
[23] A. Raghavan, C.E.S. Cesnik, Review of guided-wave structural health monitoring, *Shock and Vibration Digest* 39 (2) (2007) 91–114.
[24] J.L. Rose, Guided wave nuances for ultrasonic nondestructive evaluation, *IEEE Transactions on Ultrasonics, Ferroelectrics, and Frequency Control* 47 (3) (2000) 575–583.
[25] H. Sohn, S.J. Lee, Lamb wave tuning curve calibration for surface-bonded piezoelectric transducers, *Smart Materials and Structures* 19 (2010) 015007.
[26] Z. Su, L. Ye, Y. Lu, Guided Lamb waves for identification of damage in composite structures: a review, *Journal of Sound and Vibration* 295 (3–5) (2006) 753–780.
[27] L. Wang, F.G. Yuan, Damage identification in a composite plate using prestack reverse-time migration technique, *Structural Health Monitoring: An International Journal* 4 (2005) 195–211.
[28] M.M. Abdel Wahab, G. De Roeck, Damage detection in bridges using modal curvatures: application to a real damage scenario, *Journal of Sound and Vibration* 226 (2) (1999) 217–235.
[29] M.S. Cao, P.Z. Qiao, Novel Laplacian scheme and multiresolution modal curvatures for structural damage identification, *Mechanical Systems and Signal Processing* 23 (2009) 1223–1242.
[30] P. Cornwell, S.W. Doebling, C.R. Farrar, Application of the strain energy damage detection method to plate like structures, *Journal of Sound and Vibration* 224 (2) (1999) 359–374.
[31] E. Sazonov, P. Klinkhachorn, Optimal spatial sampling interval for damage detection by curvature or strain energy mode shapes, *Journal of Sound and Vibration* 285 (2005) 783–801.
[32] A. Gentile, A. Messina, On the continuous wavelet transforms applied to discrete vibrational data for detecting open cracks in damaged beams, *International Journal of Solids and Structures* 40 (2) (2003) 295–315.
[33] A. Messina, Refinements of damage detection methods based on wavelet analysis of dynamical shapes, *International Journal of Solids and Structures* 45 (14–15) (2008) 4068–4097.
[34] M. Rucka, K. Wilde, Application of continuous wavelet transform in vibration based damage detection method for beams and plates, *Journal of Sound and Vibration* 297 (2006) 536–550.
[35] Q. Wang, X.M. Deng, Damage detection with spatial wavelets, *International Journal of Solids and Structures* 36 (23) (1999) 3443–3468.
[36] N. Wu, Q. Wang, Experimental studies on damage detection of beam structures with wavelet transform, *International Journal of Engineering Science* 49 (3) (2011) 253–261.
[37] S. Zhong, S.O. Oyadiji, Detection of cracks in simply-supported beams by continuous wavelet transform of reconstructed modal data, *Computers and Structures* 89 (2011) 127–148.
[38] M.S. Cao, L. Cheng, Z. Su, H. Xu, A multi-scale pseudo-force model in wavelet domain for identification of damage in structural components. Mechanical Systems and Signal Processing. http://dx.doi.org/10.1016/j.ymssp.2011.11.011.
[39] P.Z. Qiao, W. Fan, A 2-D continuous wavelet transform of mode shape data for damage detection of plate structures, *International Journal of Solids and Structures* 46 (25–26) (2009) 4379–4395.
[40] X.Q. Zhu, S.S. Law, Wavelet-based crack identification of bridge beam from operational deflection time history, *International Journal of Solids and Structures* 43 (7–8) (2006) 2299–2317.
[41] S. Mallat, *A Wavelet Tour of Signal Processing*, Academic Press, San Diego, 2008.
[42] J.A. Nelder, R. Mead, A simplex method for function minimization, *The Computer Journal* 7 (1965) 308–320.